ELSEVIER

Dynamics of Atmospheres and Oceans 26 (1997) 95–130

dynamics of atmospheres and oceans

A one-dimensional model for the parameterization of deep convection in the ocean

T. Paluszkiewicz [a,*], R.D. Romea [b]

[a] Pacific Northwest National Laboratory, 1529 W. Sequim Bay Road, Sequim, WA 98382, USA
[b] STI Optronics, 2755 Northup Way, Bellevue, WA 98004, USA

Received 12 April 1994; revised 5 December 1995; accepted 17 June 1996

Abstract

A one-dimensional penetrative plume model has been constructed to parameterize the process of deep convection in ocean general circulation models (OGCMs). This research is motivated by the need for OGCMs to better model the production of deep and intermediate water masses. The parameterization scheme takes the temperature and salinity profiles of OGCM grid boxes and simulates the subgrid-scale effects of convection using a one-dimensional parcel model. The model moves water parcels from the surface layer down to their level of neutral buoyancy, simulating the effect of convective plumes. While in transit, the plumes exchange water with the surrounding environment; however, the bulk of the plume water mass is deposited at the level of neutral buoyancy. Weak upwelling around the plumes is included to maintain an overall mass balance. The process continues until the negative buoyant energy of the one-dimensional vertical column is minimized. The parameterized plume entrainment rate, which plays a central role in the parameterization, is calculated using modified equations based on the physics of entraining buoyant plumes. This scheme differs from the convective adjustment techniques currently used in OGCMs, because the parcels penetrate downward with the appropriate degree of mixing until they reach their level of neutral stability. © 1997 Published by Elsevier Science B.V.

1. Introduction

The present study describes the development of a penetrative plume parameterization scheme and initial testing of the parameterization in an ocean general circulation model (OGCM). The penetrative plume scheme was developed as a one-dimensional, stand-

* Corresponding author.

0377-0265/97/$17.00 © 1997 Published by Elsevier Science B.V.
PII S0377-0265(96)00482-4

alone model to facilitate testing, then was simplified to a parameterization scheme for incorporation in an OGCM.

Deep convective events in the ocean, especially in regions where bottom water is formed, are of particular importance to the Earth's climate. Buoyancy-driven convective overturning occurs in localized areas and is a violent, relatively short-lived event with vertical scales ultimately limited by the ocean depth. This process transports and mixes water over many hundreds of meters during a time period of hours (Aagaard and Carmack, 1989). Where this process occurs, the across-isopycnal advection gives rise to bottom water formation and controls the vertical structure of deep water masses. The formation of deep water occurs on scales that are not resolved by OGCMs; consequently, in these models and others of this type, the process is parameterized. Existing OGCMs use a convective adjustment scheme to remove the gravitational instability resulting from buoyancy losses at the ocean surface and other causes of convective instability. Studies show that the thermohaline circulation is sensitive to the sites and amount of convection as well as to the convective parameterization (Smith, 1989). Holland (1979) discussed the importance of convective adjustment to climate simulations, noting that the convective adjustment scheme was equal in importance to the eddy diffusivity parameterization. Recent work has shown that the convective schemes influence the stability of the thermohaline circulation during the transition from restoring to mixed boundary conditions (Marotzke, 1991; Weaver and Sarachik, 1991). Several forms of convective adjustment schemes exist and include the following: the basic (standard) scheme (Bryan, 1969; Semtner, 1974; Cox, 1984), an implicit vertical diffusion scheme (Cox, 1984; Killworth, 1989), and a 'complete' adjustment scheme (Marotzke, 1991; Yin and Sarachik, 1994). The basic concept of the convective adjustment scheme is that when water column instabilities occur, the temperature and salinity are adjusted to make the water column neutrally stable. Heat and salt are conserved, and a new adjusted temperature and salinity are returned.

In the simplest convective adjustment schemes (standard), the amount of instability that is removed from each profile is determined by the number of adjustment iterations that the user specifies. To invoke the convective adjustment, density at two vertically adjacent grid points is compared, and if it differs, the temperature and salinity are mixed until the density at the grid points is neutrally stable with respect to both. Killworth (1989), Smith (1989), and Marotzke (1991) showed that residual instabilities are possible with the scheme, because the finite number of iterations does not completely remove instabilities.

The implicit vertical diffusion scheme tests the stability between adjacent grid points and uses a large vertical diffusivity if the profile is unstable. This technique was adopted to remove residual instabilities, but it is computationally expensive and less efficient in finding the final boundaries of the convectively adjusted region (Yin and Sarachik, 1994).

Marotzke (1991) and Yin and Sarachik (1994) each developed a 'complete' adjustment scheme that uses a locally iterative method to determine the upper and lower boundaries of each convectively adjusted region, while keeping the instantaneous adjustment within each unstable region. The physics of the two models is the same, but the method of local iteration differs. Yin and Sarachik (1994) found that the complete removal of instabilities leads to different thermohaline variability when they used a model with their new scheme to look at interdecadal thermohaline instabilities.

These parameterizations, when used in climate simulations, enforce an implicit assumption that it is not necessary to capture the timing or effects of the mechanisms of turbulent mixing in detail. The fact that these parameterizations only remove static stability is unimportant if they adjust the ocean to the correct state. Skyllingstad et al. (1991) showed that the convective adjustment in the Community Modeling Effort (CME) did not mix deep enough to produce realistic water masses (greatest depths 700–900 m) and extended over unrealistically large regions of the Labrador Sea, and the tracer age indicated that it took on the order of 1 year to bring the tracer to depth. These discrepancies between the simulations and observation could have resulted from other difficulties in the model in conjunction with the convective adjustment scheme. Observations from Clarke and Gascard (1983) showed that convection occurs in isolated patches, penetrates to 1500 m, and happens in a matter of days. Smith (1989) reported that the 'standard' convective adjustment scheme is sensitive to both vertical grid structure and model time step. Although deeper penetration can be accomplished using a large number of convective adjustment interactions, this cannot be done without significant vertical and horizontal mixing in intermediate waters. Consequently, the methods of convective adjustment commonly used neither produce realistic vertical density structure nor create the correct quantity of deep water. Further, they may not reflect the correct timing. In their numerical study of deep convection, Sander et al. (1995) found that convective adjustment from OCGMs could simulate average temperatures fairly but that the dynamics could not be represented. They concluded that 'convective adjustment' could be an 'adequate formalism whenever small-scale dynamics play a minor role'; however, the vertical advective transport of any trace will be suppressed (Sander et al., 1995). These deficiencies prompted a re-examination of the convective adjustment scheme to build a more physically based parameterization that accomplishes both shallow convective adjustment and deep penetrative convective mixing.

The Ocean Penetrative Plume Scheme (OPPS) has the capability to parameterize the process of deep open-ocean convection in a vertical grid column of an OGCM. The goal of our research is to improve OGCM simulations by including the physics of deep penetrative convection (thermobaric convection) and deep water formation, without adding the complexity of a turbulence model or large-eddy simulation (LES). Accordingly, requirements for the model are the following: the essential physics must be parameterized in an OGCM grid volume; the code must be compact and fast; the model should interface seamlessly with the OGCM from time step to time step. The last requirement implies that the OGCM and the parameterization interact column by column only through the state variables $\theta(z)$ and $S(z)$, where θ is potential temperature, S is salinity, and z is a vertical coordinate. The parameterization needs to rearrange the thermodynamic variables vertically, consistent with vertical stability requirements, but without 'memory' from time step to time step or from grid column to grid column.

Parameterization schemes for deep convective activity in the atmosphere have been used in the meteorological community for many years (e.g. Kuo, 1974; Fritsch and Chappell, 1980). The argument in support of such schemes is identical to that for the oceanic case: because the horizontal scale of cumulus clouds is much smaller than the grid scale used in representing large and mesoscale flows, the influence of the small-scale convective motions can be incorporated in the large-scale equations parametrically. We reviewed the atmospheric parameterization schemes for penetrative convection and derived a similar set of equations for the oceanic case, accounting for the fundamental differences between the atmosphere and the ocean. For example, the equation of state for the ocean replaces the equations governing atmospheric water vapor and its behavior; also, the entrainment of momentum is more important for the ocean. Independently, but in parallel to our work, Alves (1995) reviewed concepts of atmospheric convection parameterization and, with an approach similar to that presented here, developed an ocean plume model for parameterization of deep convection.

In the next section, we discuss some aspects of the physics of deep convection as they relate to the one-dimensional parameterization, including the basic scaling and the observational evidence. In Section 3, we present the details of OPPS, including a description of the model, the entrainment hypothesis, and tests of the model under thermobaric and nonthermobaric conditions. A discussion of the major results and implications for future work is presented in Section 4.

2. The physics of deep convection

2.1. Oceanographic background

Deep convection in the ocean is important in bottom water formation. Of particular importance is the need to distinguish processes in which downward vertical motion, rather than water mass transformation, governs (Solomon, 1974; Carmack, 1990). Two types of convection have been linked with bottom water formation: near-boundary sinking and deep penetrative sinking in the open ocean. We are concerned with the latter. The conditions under which this occurs have been described by Sankey (1973) and Killworth (1979, 1983) as well as others. During the preconditioning phase, a background of low static stability is created. A combination of atmospheric cooling and salinization, together with a background cyclonic geostrophic circulation, weakens the stratification. The cyclonic circulation causes doming of the isopycnals, and deeper waters are exposed to further cooling. Intense and rapid surface-buoyancy forcing through cooling and evaporation trigger the surface instability. Surface water becomes denser than deeper waters; as a consequence, parcels of water descend with vertical velocities of 10–15 cm s^{-1} with vigorous mixing. In the Mediterranean, the location of the preconditioned gyre is determined by the localized topographic feature and its relationship with the atmospheric forcing (Sankey, 1973; Madec and Crepon, 1991). In contrast, the preconditioning of the Greenland Sea gyre is related to the withdrawal of the seasonal ice and the local wind stress curl (Rudels et al., 1989; Jonsson, 1991; Schott et al., 1993). Visbeck et al. (1995) showed that preconditioning is also affected by wind-driven ice drift, and that the freshwater balance is related to the ice dynamics and thermodynamics.

The mixing phase occurs in locations where preconditioning has been active. The preconditioning occurs in late autumn and early winter; the mixing phase is believed to occur in late winter. In the sinking and spreading phase, the newly formed dense waters equilibrate with the surroundings and spread horizontally.

Deep convection occurs primarily in the Greenland Sea, the Labrador Sea, the Weddell Sea, and the Mediterranean Sea (Killworth, 1983; Carmack, 1990; Heinze et al., 1990; Rhein, 1991; Visbeck et al., 1995). Estimates of the amount of deep water formed in open ocean deep convection are in the range of $5-10 \times 10^6\,m^3\,s^{-1}$; this is of the same order of magnitude as the estimates of deep water produced near ocean boundaries, i.e. ($7-10 \times 10^6\,m^3\,s^{-1}$), although both estimates are extremely crude.

We are concerned here with modeling the localized and nonstationary deep penetrative sinking events in the open ocean. Oceanic deep penetrative convection is caused by instability of the water column to vertical displacements in a manner analogous to atmospheric moist convection, where the atmosphere becomes unstable to overturning through a deep layer, with additional instability provided through the release of latent heat. In the oceanic case, the additional source of instability (in addition to the cooling and evaporation at the surface) arises through the nonlinear relationship between pressure and density. When relatively cold, fresh, near-surface water sinks, it can become denser than the surrounding deep water because of variations in the compressibility of seawater with pressure and salinity (i.e. thermobaric effects; Aagaard and Carmack, 1989). The full equation of state is required to correctly resolve the thermobaric effects that are associated with deep plumes, particularly at high latitudes or in the deep ocean (Sander et al., 1995; Denbo and Skyllingstad, 1996).

2.2. Previous work: observations, basic scales, and processes

Observations of deep convection, together with theory and numerical and laboratory modeling of deep convection, have established the major features and scales of the process. Through this work, a vocabulary has evolved to define the major features of a deep convective region. The major features and the corresponding hierarchy of scales for deep convective processes are the following: plumes, chimneys, and rim currents (Jones and Marshall, 1993).

Plumes are fundamental, convectively driven vertical motions. Whereas shallow convection, or mixed-layer deepening, has scales of hundreds of meters (Killworth, 1983; Guest and Davidson, 1991), deep convective plumes have vertical scales of 1–2 km (Gascard and Clarke, 1983), horizontal scales of 100 m to 1 km, and associated vertical velocities of $2-10\,cm\,s^{-1}$ (Rudels et al., 1989; Schott and Leaman, 1991; Carsey and Garwood, 1993; Roach et al., 1993; Schott et al., 1993; Garwood et al., 1994; Denbo and Skyllingstad, 1996). Time scales associated with convective plumes are several hours to several days (Rudels et al., 1989; Roach et al., 1993). The convective plumes are apparent as isolated regions of vertically coherent, downward velocity in the vertical velocity fields measured by acoustic doppler current profilers (ADCPs).

Schott et al. (1993) observed active convective elements with horizontal scales of 1 km or smaller in the Greenland Sea. The vertical velocities associated with the plumes range from 2 to $7\,cm\,s^{-1}$ (Gascard, 1991) in the Labrador Sea, and up to $3.5\,cm\,s^{-1}$ with vertical velocity burst of up to $6-8\,cm\,s^{-1}$ in the Greenland Sea (Roach et al., 1993; Schott et al., 1993). Scott and Killworth (1991) observed small convective cells, roughly 3 km, that were consistent with the conceptual model presented by Killworth (1983). Rudels et al. (1989) observed a similar area of deep, vertically well-mixed waters. The deep oxygen observations of Rudels et al. can only be explained by relatively rapid vertical transport, with minimal mixing. The isolation of the oxygen discounts the advection of high oxygen water laterally and implies deep vertical mixing. Mixed-layer deepening and the erosion of the stratification could not explain this structure. The isolation of plumes at the base of the mixed layer (Scott and Killworth, 1991) also cannot be explained by simple mixed-layer deepening or by erosion of the density structure. These early observations could show the existence of the effects of penetrative plumes in the Arctic. Paluszkiewicz et al. (1994) described the theories and hypothesis that could be relevant to the penetrative nature of plumes in these regions.

The small scale of plumes was resolved by an array of ADCPs of 2 km width in the 1992 Mediterranean measurements (Schott et al., 1994). Vaughn and Leaman (1995) reviewed the data from observations and modeling of the Gulf of Lions in 1987 (Schott et al., 1988; Leaman and Schott, 1991; Schott and Leaman, 1991) and found that the region was organized into small-scale (of the order of 1 km) cells embedded in a larger-scale (of the order of 50 km) homogeneous ‘patch’. Their analysis showed that these cells provide the necessary turbulence for efficient vertical mixing of the water column and for removal of the ambient stable stratification. They clarified that these cells (‘plumes’, in this paper) are not directly performing the net volume transport downward (the soda-straw conceptual model), but that they do contribute to the transport of fluid properties such as heat, energy, and chemical tracer concentration.

Recent high-resolution numerical studies (Jones and Marshall, 1993; Garwood et al., 1994; Paluszkiewicz et al., 1994; Send and Marshall, 1995; Sander et al., 1995; Denbo and Skyllingstad, 1996) showed that open-ocean convective events consist of atmospherically forced regions of the ocean containing ensembles of penetrative turbulent plumes. The modeled plume ensembles have vertical scales limited ultimately by the total ocean depth, with horizontal scales of 10–100 km, defined by the atmospheric forcing. The individual plumes, when resolved properly, have horizontal scales of 200–500 m and descend vertically while mixing over depths of 200 m to 1 km. Both the numerical and observation studies indicate that plumes act as mixing agents rather than as downward carriers of mean flow (Schott et al., 1993; Send and Marshall, 1995; Vaughn and Leaman, 1995). It is the turbulent nature of these plumes that provides the energy for their mixing function (Deardorff and Willis, 1985; Vaughn and Leaman, 1995); it is the entrainment that the plumes generate that is the mechanism for the exchange of properties (Turner, 1973).

Chimneys are regions of nearly homogenous water embedded in a region of stronger stratification. The deep mixed layers are formed by the action of an ensemble of plumes active over a large region. Their vertical extent is the maximum penetration depth of the ensemble of plumes, which could in some cases reach all the way to the sea floor. Time scales (several days) for these features are associated with geostrophic adjustment and baroclinic instability. Chimneys have been found in the Greenland Sea (Scott and Killworth, 1991; Johannessen et al., 1991), Labrador Sea (Gascard and Clarke, 1983), Mediterranean Sea (Sankey, 1973), and Weddell Sea (Gordon, 1978; Muench, 1991).

Table 1
Scaling for plumes and chimneys for deep convective processes

Scale	Plumes	Chimneys
L_z (km)	0.2– D	$(D/2)$– D
L_x (km)	0.2–1.0	10–100
w (cm s^{-1})	5–10	Not applicable
dt	1–10 h	1–2 days
R_x	1.5–3.8	< 0.08
dz (km)	0.8	≈ 0.4

L_x and L_z are horizontal and vertical length scales, respectively; w is characteristic vertical velocity; dt is characteristic time scale; R_x $(= w/fL_x)$ is the horizontal Rossby number; dz is the vertical scale for which the 'plume' Rossby number $(R_0 = w/f dz)$ equals unity. The Coriolis parameter f is computed at 65° latitude. D is total ocean depth (approximately 2 km), and the Rossby radius scale is approximately 10 km.

Gascard (1991) provided a summary of the characteristics of chimneys in each of these regions.

The rim current, or the density-driven current, is found near the front between the chimney and the surrounding fluid. Around the edge of a chimney flows the geostrophic rim current, which is baroclinically unstable and breaks into eddies, which transport water between the chimney and the surrounding environment (Gascard and Clarke, 1983; Gascard, 1991; Jones and Marshall, 1993; Send and Marshall, 1995).

Numerical and tank modeling experiments have illustrated the role of rotation in the process of deep convection and the degree to which the plume, chimney, rim current, and embedded eddies are affected by rotation (Fernando et al., 1989; Boubonov and Golitsyn, 1990; Maxworthy and Narimousa, 1994). The scaling for rotation is of interest for parameterizing the effect of rotation on individual plume elements. Table 1 summarizes these scales. It also lists R_x, the Rossby number, defined with the horizontal length scale, and dz, the vertical length scale for which the 'plume' Rossby number (defined with the vertical length scale) equals unity (i.e. $R_0 = w/f dz \approx 1$). As R_0 approaches unity, the effects of rotation become important.

Table 1 shows that whereas regions comprising ensembles of plumes are clearly dominated by the effects of rotation, individual plumes of limited vertical extent may or may not be strongly affected. For $R_0 > 1$ (i.e. $z < dz$), and assuming $dz < D$ (the ocean depth), the plume evolves according to entrainment scaling, with buoyancy flux and vertical stability as the primary driving factors. Denbo and Skyllingstad (1996) examined the effects of rotation on penetrative convection using an LES model. In the absence of rotation, vertical motions are more energetic and the convective fields are organized on a larger horizontal scale (1–10 km). The diameters of plumes under the influence of rotation are smaller (300–500 m) than the diameters of plumes without rotation (1000 m). Analysis of numerical model runs shows that plumes with rotation are smaller by 10–20% than those without rotation (Denbo and Skyllingstad, 1996). We are currently examining the relationship of the radius of the plume size to a geophysical parameter, such as the Rossby radius, by compiling observations and numerical experiments (following the approach of Denbo and Skyllingstad) in the various convective regions (MEDOC, Labrador Sea, and Antarctic).

It is useful to examine the conditions under which it is justified to neglect rotational effects. It should be noted that the plumes considered here have horizontal scales of 100–500 m and vertical scales of 200–2000 m. These are not the 'chimneys' reported by others (e.g. Jones and Marshall, 1993), where ensembles of plumes define an area with horizontal scale of greater than 10 km and where rotation is clearly important.

Fernando and Ching (1993) examined the effects of background rotation on long, thin, turbulent line plumes associated with polar lead, and determined experimentally that individual lead-generated plumes are affected by background rotation after descending to a depth of $h_c = 3.2 q_0^{1/3}/\Omega$, where q_0 is the surface buoyancy flux per unit length and Ω is the background rotation. Using typical values for the Arctic, they obtained h_c approximately 3500 m. More recently, Maxworthy and Narimousa (1994) reported results from laboratory experiments on turbulent convection into a homogeneous rotating fluid, where they found that the transition depth, where rotational effects dominated the turbulence, occurred for $h_c \approx 12.7 B_0^{1/2}/f^{3/2}$, where f is the Coriolis parameter and B_0 is the surface buoyancy flux ($m^2\,s^{-3}$). For cooling, $B_0 = (g/\rho)(\delta Q/c_p)$, where g is gravitational acceleration, ρ is the fluid density, δ is the coefficient of thermal expansion, and c_p is the heat capacity. Their results were in agreement with earlier measurements by Fernando et al. (1991), yielding estimates for the Arctic of $h_c > 3$ km.

The effect of rotation on individual plumes is included in the one-dimensional model by choosing an initial radius that corresponds to observations (Schott et al., 1993) and to model results (Denbo and Skyllingstad, 1996). Ideally, the parameterization of the effect of rotation could be adaptive, using the correct relationship of plume diameter and latitude (Rossby radius). In the design of this parameterization, we assume that the OGCM or some other lateral mixing scheme performs the larger-scale adjustment under gravity and rotation to account for the chimneys that can form as a result of parameterized adjustment in individual grid columns.

3. The OPPS model

3.1. Parameterization scheme

The formulation of the parameterization scheme follows the same general approach as described by Fritsch and Chappell (1980) for convective cumulus parameterization in the atmosphere, although the equations have been recast, rederived, and rescaled for the oceanic case. The vertical column of values for potential temperature θ and salinity S that are handed to the plume model by (for example) an OGCM are assumed to be grid-volume-averaged variables (averaged in space over a grid volume and in time over an OGCM time step). A measure of the available buoyant energy (ABE), which defines the vertical stability of a fluid column, controls the amount of plume activity in the grid column. A plume model based on an entrainment hypothesis together with conservation of mass and momentum for fluid parcels moved vertically is used to estimate the vertical structure of the convective plume mass flux downward, which is required to reduce the ABE to zero in a finite time τ_p. Compensating upward motion in the environment follows from mass continuity, so that the vertical structures of environmental temperature and salinity changes are also specified by the plume model. The grid-point variables are reconstructed as area-weighted means of plume and environment values using Eq. (1). In practice, the OPPS replaces any convective adjustment scheme used and can be inserted in the same place in the OGCM code; consequently, OPPS will perform all the convective adjustment.

Grid-volume averaging in OPPS occurs as follows. For unstable conditions, an ensemble of plumes is assumed to be active in a grid volume. A grid-volume averaged variable $\bar{\phi}$ can be decomposed into

$$\bar{\phi} = (1 - \sigma_p)\phi_e + \sigma_p \phi_p \tag{1}$$

where ϕ represents a dependent variable, an overbar denotes a grid-volume-averaged variable, ϕ_e represents the value of the dependent variable outside the plumes in the environment, and ϕ_p is the value in the plumes. The parameter σ_p represents the fractional coverage of a horizontal grid interval by active plumes required to reduce the ABE to zero. The choice of σ_p is not immediately intuitive or obvious from the basic physics of convection; consequently, the scheme iteratively adjusts σ_p until the ABE is reduced. We have reviewed the high-resolution model simulations from Denbo and Skyllingstad (1996) to determine the fractional plume coverage of their model domain. The value of σ_p can be estimated by evaluating the radius (chosen to parameterize rotation) of an average plume to the grid size of the model. It should be noted that whereas σ_p represents the fractional area occupied by an ensemble of many plumes, the entrainment rate is linked to the radii of individual plumes. All the individual plumes in a grid element are assumed to be alike, so that σ_p corresponds essentially to the summed areas of a number of plume 'units'.

Our motivation to include the plume physics in this parameterization came from the basic work of Turner (1973) and Deardorff and Willis (1985), which shows theoretically, analytically, and numerically that is the convective cells (plumes) that do the turbulent mixing that accomplishes deep convection. Following this, we were motivated by the success of atmospheric modelers in representing convection by taking a plume approach. Finally, there is a great agreement in the numerical modeling results of Garwood (1991), Jones and Marshall (1993), Sander et al. (1995) and Denbo and Skyllingstad (1996) that plumes evolve as the convectively forced mixing elements.

3.2. *Stability*

The stability of a parcel of fluid in grid volume I with respect to the grid volume $I+1$ below it is obtained by moving the parcel adiabatically from $z(I)$ to $z(I+1)$, where z is a vertical coordinate, and comparing potential densities ρ:

$$\rho(i)_d - \rho(i+1) - \Delta\rho \begin{cases} \prec & 0; \quad \text{stable} \\ \succ & 0; \quad \text{unstable} \end{cases} \tag{2}$$

where the subscript d refers to the adiabatic displacement and $\Delta\rho$ simulates a stability threshold associated with the inhibiting effects of viscosity and rotation.

In the ocean, the thermodynamics are simpler than in the atmosphere in one respect: it is not necessary to include water vapor saturation effects. In all other aspects, the thermodynamics are more complicated. To accurately model the vertical stability of (possibly thermobarically unstable) fluid columns in the ocean, it is necessary to know accurately the equation of state of the ocean. Accordingly, we have implemented the full nonlinear equation of state, including the effect of salinity on compressibility and the thermal expansion coefficient. OPPS, when used as a stand-alone scheme, computes density and other quantities related to density by solving the full equations listed in Appendix 3 of Gill (1982); however, it uses a look-up table within the OGCM to increase speed without introducing numerical error.

3.3. The entrainment hypothesis

A fundamental parameter of the OPPS is the entrainment rate for individual plumes. Fritsch and Chappell (1980) assumed that parcels rising in cumulus clouds entrain an amount of fluid equal to their starting mass as they travel from the bottom to the top of the cloud; that is, the cloud increases its mass by 100% from cloud base to cloud top. They defended this choice by appealing to observations of cumulus clouds (e.g. Byers, 1951). For the oceanic case, there are limited observations of thermobaric plumes to derive an entrainment rate; therefore, we must draw on theoretical and modeling results. In this section, we review the turbulent entrainment hypothesis as it relates to individual plumes in thermobarically unstable environments.

The entrainment hypothesis simply states that the mean inflow velocity across the edge of a turbulent flow is assumed to be proportional to a characteristic velocity. This assumption applies to a wide range of scales (Turner, 1973; List, 1982). In particular, for 'point-source' plumes penetrating into a stable environment (buoyancy frequency N^2 is constant and positive), this hypothesis leads to the similarity solution illustrated in Fig. 1, which essentially reproduces Fig. 6.17 of Turner (1973). Distance from the point source is measured upward in Fig. 1 (i.e. the atmospheric case). Up to a nondimensional value of about $z = 2.0$, the plume spreads out linearly with distance from the source, and the vertical velocity decreases as the plume mass flux increases owing to entrainment. It should be noted that the plume 'overshoots' above $z = 2.0$ (the buoyancy flux is negative) and spreads out rapidly above $z = 2.4$.

More complicated entraining jet models for cumulo-nimbus updraughts (e.g. Squires and Turner, 1962; Kessler, 1988), which result from deep atmospheric instability, show both acceleration and narrowing near cloud base. Similarly, three-dimensional model results (Denbo and Skyllingstad, 1996) for thermobaric plumes in the ocean indicate that, at least initially, the plumes become narrower, and the vertical velocity increases with distance from the upper unstable layer.

With these results in mind, we develop a simple model for individual thermobaric plumes based on the entrainment hypothesis, but with mixing of salt and temperature for realistic thermobaric profiles, and with the full nonlinear equation of state for seawater. We start with the standard equations for the conservation of mass and momentum for buoyant entraining plumes, following the work and equations of Turner (1973), to derive an entrainment relationship for oceanic convective plumes where stratification and a full

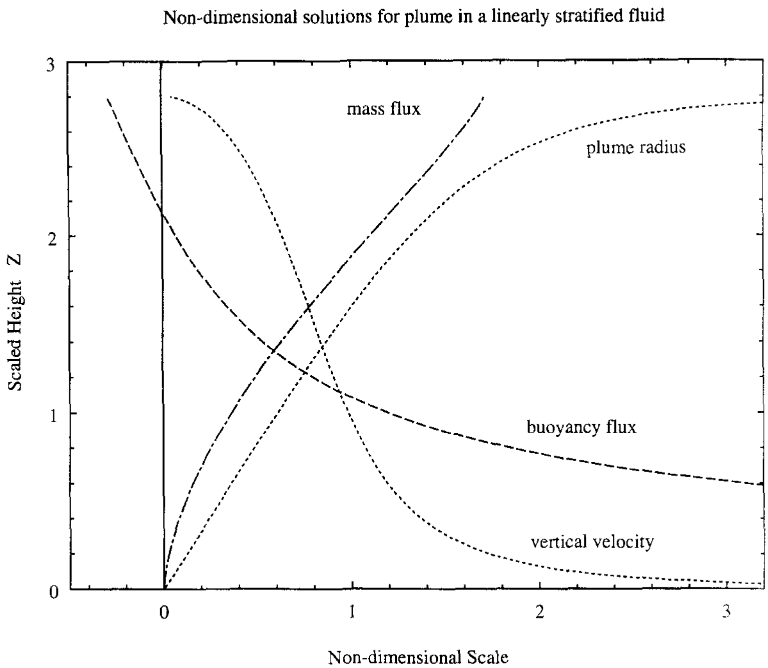

Fig. 1. Non-dimensional solutions for plumes in a linearly stratified (constant N^2) fluid (a recalculation of Turner (1973), Fig. 6.17). The plot considers a virtual point source at the origin. In a stable environment, the plume spreads linearly, and mass flux increases until the point where the fluid begins to flow out sideways. The orientation is appropriate for the atmospheric case.

equation of state are important. The entrainment hypothesis (Turner (1973) Eq. (6.1.4), p. 171) provides the starting point, with the inclusion of a nonzero N:

$$\frac{dM}{dz} = 2\alpha w_p b \rho_e \tag{3}$$

which implies that plume mass flux M varies with distance z downward at a rate proportional to the downward plume velocity w_p and the plume radius b. The constant of proportionality is α, and ρ_e is the density of the environment (the entrained fluid). We will take $\alpha = 0.10$, a value that is likely to be within 15% of the true value (Turner, 1962, 1963, 1986). The plume mass flux is given by

$$M = b^2 w_p \rho_p \tag{4}$$

where a 'top-hat' profile is assumed; that is, at a given depth all the properties are assumed to be constant with radius in a plume.

The expression for the variation of momentum flux owing to buoyancy forces for a 'narrow' plume (b much less than vertical extent) is

$$\frac{d}{dz}(M w_p) = g b^2 (\rho_p - \rho_e) \tag{5}$$

The variations of potential temperature θ_p and salinity S_p in the plume are given by

$$\frac{d\theta_p}{dz} = (\theta_e - \theta_p)\frac{1}{M}\frac{dM}{dz} \tag{6}$$

$$\frac{dS_p}{dz} = (S_e - S_p)\frac{1}{M}\frac{dM}{dz} \tag{7}$$

Eq. (6) and Eq. (7) define the changes in potential temperature and salinity of a fluid parcel, with mass flux M descending adiabatically while entraining mass at a rate of dM/dz. Eq. (6) is equivalent to Eq. (18) of Fritsch and Chappell (1980) for potential temperature of an ascending parcel in a cumulus cloud. Eq. (7) is the oceanic analog to describe the role of salinity. Finally, density is computed with the complete equation of state for seawater

$$\rho = \rho(\theta, S, p) \tag{8}$$

where the pressure p is computed hydrostatically with

$$\frac{dP}{dz} = -g\rho_e \tag{9}$$

Eq. (3), Eq. (4) and Eq. (5) can be combined to yield equations for the evolution of the plume radius and for the kinetic energy:

$$\frac{db}{dz} = 2\alpha - \frac{bg'}{2w_p^2} \tag{10}$$

$$\frac{d}{dz}\left(\frac{1}{2}w_p^2\right) = \frac{-4\alpha\left(\frac{1}{2}w_p^2\right)}{b} + g' \tag{11}$$

where g' is the 'reduced gravity':

$$g' = \frac{g(\rho_p - \rho_e)}{\rho_e} \tag{12}$$

In both Eq. (10) and Eq. (11), the first term on the right-hand side represents spreading and deceleration owing to entrainment of environmental fluid, and the second term represents narrowing and acceleration owing to buoyancy forcing. This implies that the plume will always spread more slowly than predicted by simply including the effect of entrainment, and could in fact become narrower with depth under certain conditions, such as a mid-depth source of buoyant energy. We have neglected the term $(b/2\rho)(d\rho/dz)$ because it is eight orders of magnitude smaller than the other terms. This scaling is presented in Appendix A.

3.4. Results of the entrainment model for individual plumes

Once the background fields $\theta_e(z)$ and $S_e(z)$ have been specified, and a value has been chosen for α, Eqs. (3)–(8) form a closed set, which can be solved numerically with

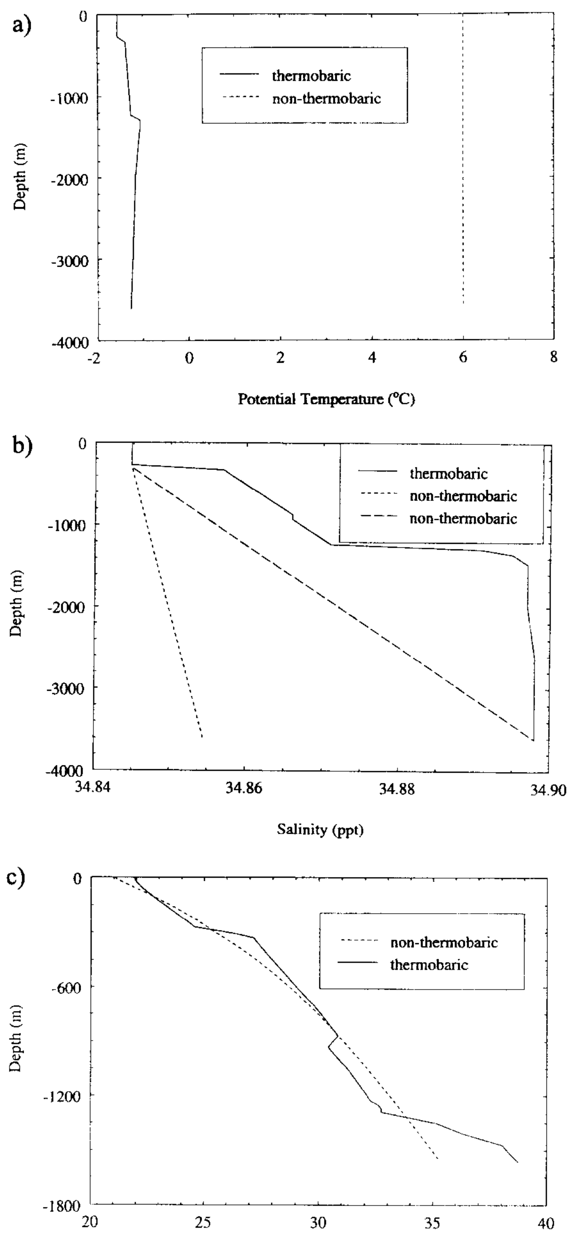

Fig. 2. (a) Potential temperature, (b) salinity profiles, and (c) density profiles used in the testing of the entrainment model. The continuous line profiles of temperature and salinity are representative of thermobarically unstable conditions under the influence of cooling. The dotted line is a very weakly stratified but thermobarically stable profile. The dashed line is a thermobarically stable salinity profile that gives a constant N^2 profile, but that has the same salinity and temperature difference from top to bottom.

(for example) a fourth-order Runga–Kutta scheme, with initial conditions specified for plume variables: b, w_p, θ_p, and S_p. The model allows a plume to be started with its initial conditions at any depth z_p.

We ran the model for various initial plume characteristics, with a thermobarically unstable density profile (a potential temperature and salinity profile from a hydrographic

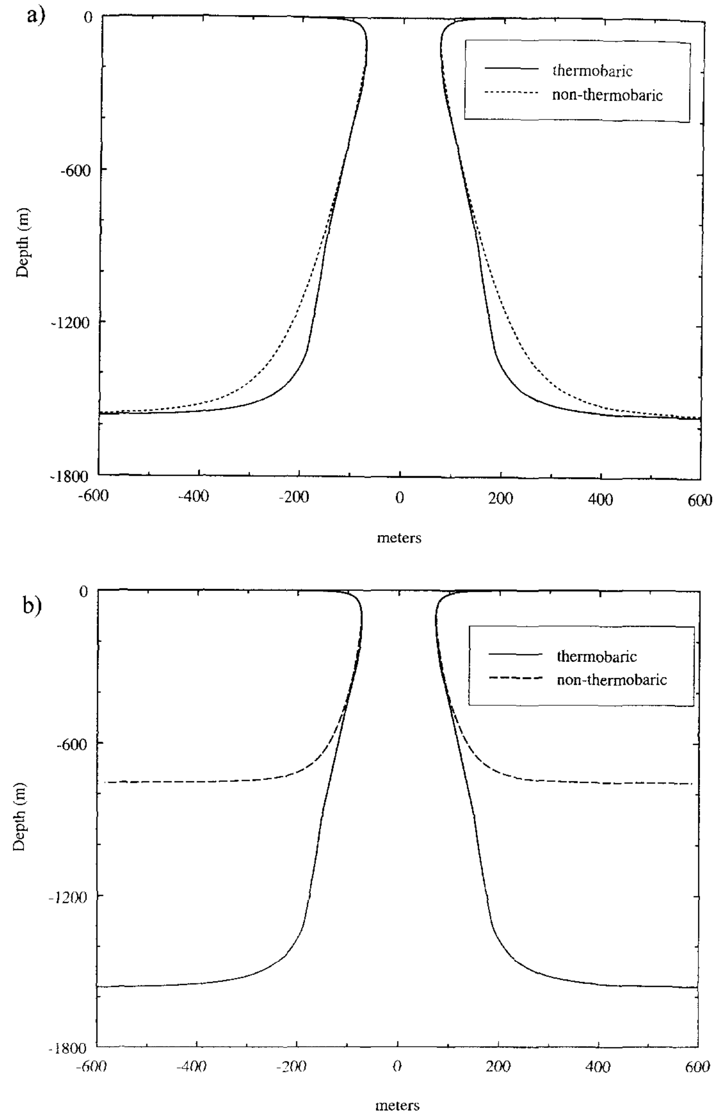

Fig. 3. Plume diameter as a function of depth for a thermobarically unstable case (continuous line) and two stable cases (dotted and dashed lines) corresponding to the profiles in Fig. 2. The plume diameter of the thermobaric case vs. the stable salt gradient where in (a) the stable salt gradient was chosen to give the same penetration depth, and in (b) the profiles were chosen to give the same salinity gradient.

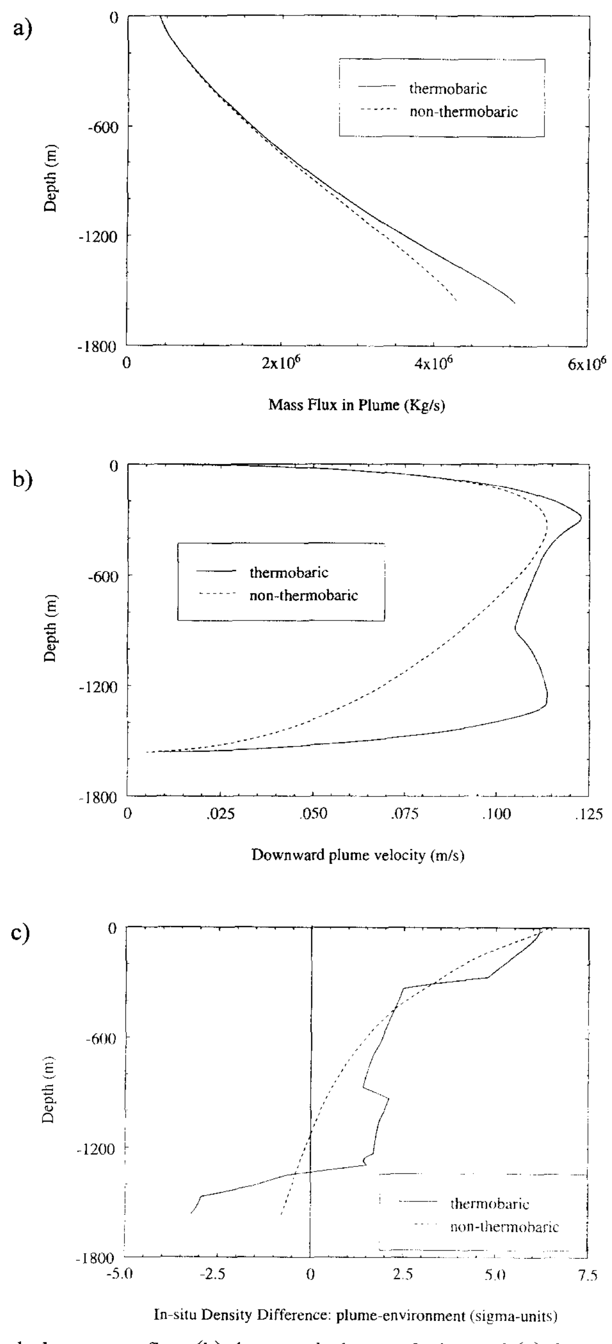

Fig. 4. (a) Downward plume mass flux, (b) downward plume velocity, and (c) downward buoyancy force (expressed as in situ density difference) for a thermobaric and non-thermobaric stratification. The non-thermobaric profile is the dotted line in Fig. 2.

station, CTD 65, in the central Greenland Sea (2°W, 74°45′N), as reported by Rudels et al. (1989)) and with a thermobarically stable profile, for comparison. Fig. 2(a), Fig. 2(b) and Fig. 2(c) show salinity, potential temperature, and density profiles, respectively, for both the stable (dashed and dotted lines) and unstable (continuous lines) cases. For both cases, there was a 300 m mixed layer at the surface. For the stable case, the potential temperature was fixed to be a constant value of 6°C, with one of two possible linearly varying salinity profiles. This yielded an approximately constant N^2 profile.

Fig. 3(a) and Fig. 3(b) show model results for plume diameter as a function of depth for a thermobarically unstable case (continuous lines), and for two stable cases, with plumes started at the surface. The initial plume radius (200 m), downward velocity (5 cm s^{-1}), and buoyancy flux were the same for all three cases. Fig. 3(a) shows the result (dotted line), with the stable salinity gradient plotted as a dotted line in Fig. 2. This weak gradient was picked so that with the same initial conditions, both the stable and unstable profiles gave the same plume penetration depths. Fig. 3(b) shows the result (dashed line), for the stable salinity gradient plotted as a dashed line in Fig. 2(b). This gradient was picked to give the same salinity gradient from top to bottom for the stable and unstable profiles. As expected, the same salinity gradient gives a much shallower plume penetration depth for the stable profile than for the unstable profile; a much weaker stratification is required to yield the same plume penetration depths for the two cases. Fig. 3(a) illustrates the narrowing of the thermobaric plume relative to the non-thermobaric case, as it accelerates between 800 and 1400 m depth.

Fig. 4(a), Fig. 4(b) and Fig. 4(c) show the downward plume mass flux, downward plume velocity, and in situ density difference (downward buoyancy force) between

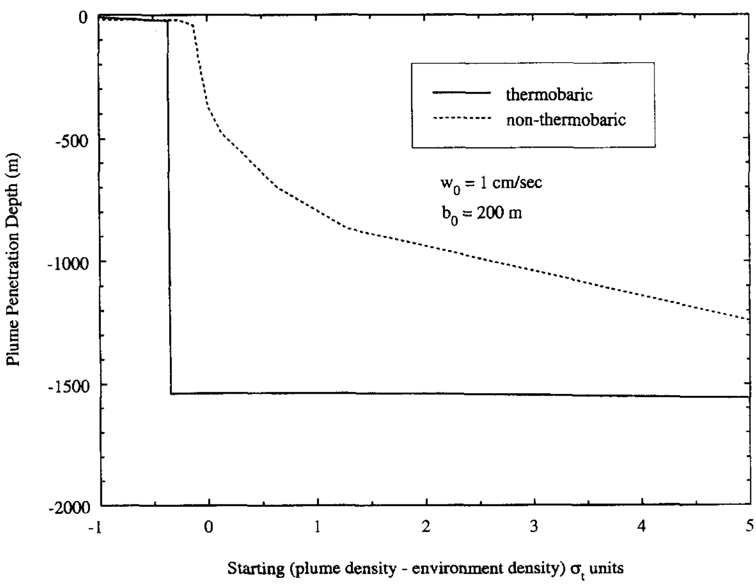

Fig. 5. Plume penetration depth vs. initial buoyancy forcing (expressed as in situ density difference) for thermobaric and non-thermobaric profiles.

plume and environment water, respectively, as a function of depth. Both plumes accelerate through the mixed layer where the buoyancy forcing is high. The non-thermobaric plume decelerates continuously below the mixed layer as the buoyancy forcing decreases with mixing of entrained environmental water with plume water. In the thermobaric case, the increased buoyancy causes an acceleration of the plume between 800 and 1200 m depth. There is little difference in the plume mass flux profiles for the two cases near the surface. However, the thermobaric plume entrains more water at depth as it accelerates relative to the non-thermobaric plume.

Fig. 5 shows plume penetration depth plotted against initial plume buoyancy forcing for both the thermobaric and non-thermobaric plumes. The buoyancy forcing is represented as plume density minus environment density, so that positive values indicate unstable conditions. The two cases exhibit very different behavior. For the thermobaric plumes, the initial downward plume velocity of 1 cm s^{-1} gives a small amount (less than 20 m) of penetration even for statically stable conditions. For statically unstable conditions, the thermobaric plumes penetrate far deeper than nonthermobaric plumes. The role of the thermobaric effect is to provide the distributed sources of energy that fuel the deeper penetration that occurs in Arctic areas of deep water formation.

3.5. Available buoyant energy (ABE)

The amount of plume activity that occurs in a model time step is governed by the driving force for the process, ABE. The vertical component of the momentum equation for the subgrid-scale perturbations in the plume downdraughts is given by Eq. (11), where g' is defined as

$$g' = g\frac{(\rho_p - \bar{\rho})}{\bar{\rho}} \tag{13}$$

By adopting Eq. (11), steady-state conditions are assumed, the subgrid-scale pressure perturbation and vertical component of rotation terms have been ignored, and the grid-averaged vertical velocity is assumed to be much smaller than vertical velocities associated with the plumes. The entrainment of momentum is included in Eq. (11).

Integrating Eq. (11) between the uppermost unstable layer (the level of free convection or LFC) and the equilibrium density level (EDL) for a parcel that is lowered without mixing gives the increase in kinetic energy (derived from buoyancy) of a parcel that falls and accelerates as it travels from its LFC to its EDL:

$$\mathrm{ABE} = \frac{1}{2}w^2(\mathrm{EDL}) - \frac{1}{2}w^2(\mathrm{LFC}) = -g\int_{\mathrm{LFC}}^{\mathrm{EDL}}\frac{\rho_p - \bar{\rho}}{\bar{\rho}}\mathrm{d}z \tag{14}$$

The condition for complete removal of ABE by plumes after time τ_p is that Eq. (14), applied to the vertical column after adjustment for the plume activity, gives ABE = 0.

3.6. Salt and heat removal

For test runs, the buoyancy flux for the model is driven by specifying a certain amount of heat flux Q and latent heat or 'salt' flux (defined as precipitation minus evaporation, $p-e$) from the upper grid volume for a given model run time step Δt. The temperature change $\Delta\theta$ owing to heat flux at the surface is computed with

$$\Delta\theta = \frac{1}{\rho c_{\mathrm{p}}}\frac{\Delta t}{\Delta z}Q \tag{15}$$

where Δz is the thickness of the surface grid volume and ρc_{p} is the heat capacity per unit volume of the seawater.

The change of salinity, ΔS, owing to the effect of the precipitation–evaporation (or melting–freezing) imbalance is computed according to

$$\Delta S = -\left[\frac{(p-e)}{\rho}\frac{\Delta t}{\Delta z}S\right] \tag{16}$$

Within the OGCM, Eq. (15) and Eq. (16) are not necessarily used. The OGCM passes OPPS the grid column profile of potential temperature and salinity, as well as the bottom depth. The surface boundary conditions of the OGCM (whether restoring, flux, or some other) modify the grid column potential temperature and salinity.

3.7. Plume characteristics

Beginning with the upper grid volume, a parcel is lowered to the next level and checked for stability with Eq. (2). If the parcel is stable, a similar test is performed on the next lower grid volume, and so on to the bottom of the grid. If the parcel is unstable, the depth-dependent entrainment rate (from top to bottom) is calculated with the entrainment hypothesis as described in Section 3.3 and Section 3.4. Values for the vertical velocity associated with the plume at the surface ($w_{\mathrm{p}}(1) \approx 0.5\,\mathrm{cm\,s^{-1}}$), the initial plume radius (100–200 m), and α (approximately 0.1), the entrainment constant, are specified as model parameters.

The parcel is lowered and mixed through vertical grid points according to

$$\phi_{\mathrm{p}}(i+1) = \frac{\phi_{\mathrm{p}}(i) + \Delta M\tilde{\phi}_{\mathrm{e}}(i)}{1+\Delta M} \tag{17}$$

where ϕ_{p} is potential temperature or salinity of the plume, and where

$$\Delta M = = \frac{M_{\mathrm{p}}(i+1)}{M_{\mathrm{p}}(i)} - 1 \tag{3.18}$$

is the fractional change in plume mass flux ($M_{\mathrm{p}}(I)$ is the plume mass flux at level I). Eq. (17) defines the potential temperature or salinity of a parcel's descending adiabatically from level I to level $I+1$ while entraining mass at a rate $K_{\mathrm{p}}(I)$ such that

$$M_{\mathrm{p}}(i) = M_{\mathrm{p}}(1)\left[1 + K_{\mathrm{p}}(i)\right] \tag{3.19}$$

The entrained fluid is contributed by the environment in a volume-weighted average of layers I and $I+1$:

$$\tilde{\phi}_{\mathrm{e}}(i) = \frac{\Delta z_{(i+1)}\phi_{\mathrm{e}(i+1)} + \Delta z(i)\phi_{\mathrm{e}}(i)}{\Delta z(i) + \Delta z(i+1)} \tag{20}$$

The procedure stops at the level where the parcel is stable with respect to the underlying fluid. The model does not currently allow 'overshooting' of plumes beyond their level of neutral density, although the behavior is described in the entrainment model of Section 3.4. Examination of the time-dependent behavior of the three-dimensional LES model (Denbo and Skyllingstad, 1996) indicates that plume water that is deposited below the neutral density level owing to overshooting 'rebounds' and spreads out in a layer at the neutral density level. The one-dimensional model crudely simulates this effect in individual grid columns by computing the total mass transported by the plume and replacing the fluid in the lowest layer reached by the plume with that amount of plume water.

The initial choice for $\sigma_p(1)$, the fractional area of plumes in the upper unstable layer, gives the starting plume mass flux:

$$M_p(1) = \rho_p(1) W_p(1) \sigma_p(1) \tag{21}$$

The fractional area covered by plumes of the remaining grid levels I is then given by

$$\sigma_p(i) = \frac{M_p(i)}{\left[\rho_p(i) W_p(i)\right]} \tag{22}$$

As we will discuss below, the value of $\sigma_p(1)$ is adjusted iteratively to reduce the ABE to zero.

3.8. Adjustment in the environment

The adjustment of the environment occurs in two stages, the unsteady plume development and the steady plume flux. Both stages depend on the choice for $\sigma_p(1)$ in the following way.

In Stage 1, during the unsteady development of the plume, fluid from the upper unstable layer moves downward and displaces lower-layer fluid upward to balance mass. The adjustment of the environment is computed by mixing salinity and potential temperature between layers.

In Stage 2, during the steady plume flux, that is, after the plume has reached its equilibrium level, the compensating upward velocity in the environment owing to the steady flux of fluid downward by the plumes is computed with

$$w_e(i) = \frac{-M_p(1)}{\rho_e(i)\left[1 - \sigma_p(i)\right]} \tag{23}$$

For this stage, the environmental variables are adjusted according to

$$\frac{\partial \phi_e}{\partial t} = -w_e \frac{\partial \phi_e}{\partial z} \tag{24}$$

3.9. Plume time scale

The model attempts to remove all the ABE in a single OGCM time step. Therefore, an adjustment process that can take 2–24 h effectively occurs in a single OGCM time step. The justification for this follows from the observation that the large-scale circulation typically takes many days or even weeks to develop thermobaric conditions, whereas the instability process is relatively short lived. Whether or not the precise timing of vertical adjustment of thermobarically unstable conditions is important on climatological time scales will be tested in a forthcoming paper on in-depth studies of the effect of using OPPS in a OGCM.

Having said this, the choice for a plume time scale τ_p is somewhat arbitrary. In terms of the adjustment of the ABE to zero, either τ_p or $\sigma_p(1)$ can be iteratively varied. In other words, many plumes can operate in a grid volume for a short period, or fewer plumes for a longer time.

The model fixes τ_p to the smaller of the following conditions:

1. The time for a fluid parcel to travel at speed w_p from the top of the plume to the bottom of the plume, shown by

$$t_p = \sum_{\text{Top grid}}^{\text{Bottom grid}} \frac{\Delta z(i)}{w_p(i)} \tag{25}$$

2. The time for the mass flux $M_p(1)$ out of the upper layer to completely replace the upper grid volume with fluid from below, shown by

$$t_p = \frac{\Delta z(1)}{w_p(1)\,\sigma_p(1)} \tag{26}$$

3.10. Overview of the numerical scheme

Fig. 6 shows a flow chart of the OPPS model as it is currently configured for test model runs. For each time step, a specified amount of heat and water $(e-p)$ is removed from the upper layer. If freezing occurs, the model run is terminated. A parcel from the upper layer is then checked for stability. If it is stable, the next lower grid volume is checked. If no unstable layers are found, control is passed to the next time step. If a parcel is unstable, it is lowered adiabatically without mixing to its level of neutral stability, and the total ABE is computed. The individual plume entrainment rate is computed using the entrainment hypothesis, and the parcel is then lowered with mixing at that rate, assuming a starting fractional plume coverage in the upper grid volume (nominally set to 0.05), until the plume either reaches the bottom of the ocean or reaches a level of neutral stability. The potential temperature and the salinity of the plume at every level are known, and the vertical plume velocity is computed. This, in turn, gives a plume time scale.

The code then enters a two-phase iterative loop where, during Phase 1, the starting downdraught area is adjusted until the ABE is reduced to zero. For the assumed plume fractional coverage σ_p, the mass flux, downdraught area, and compensating updraught owing to fluid displaced by the developing plume are determined. The change in the environment owing to the updraught is computed, and then the new grid-volume-averaged variables are calculated along with the new ABE. Normally, the first guess does

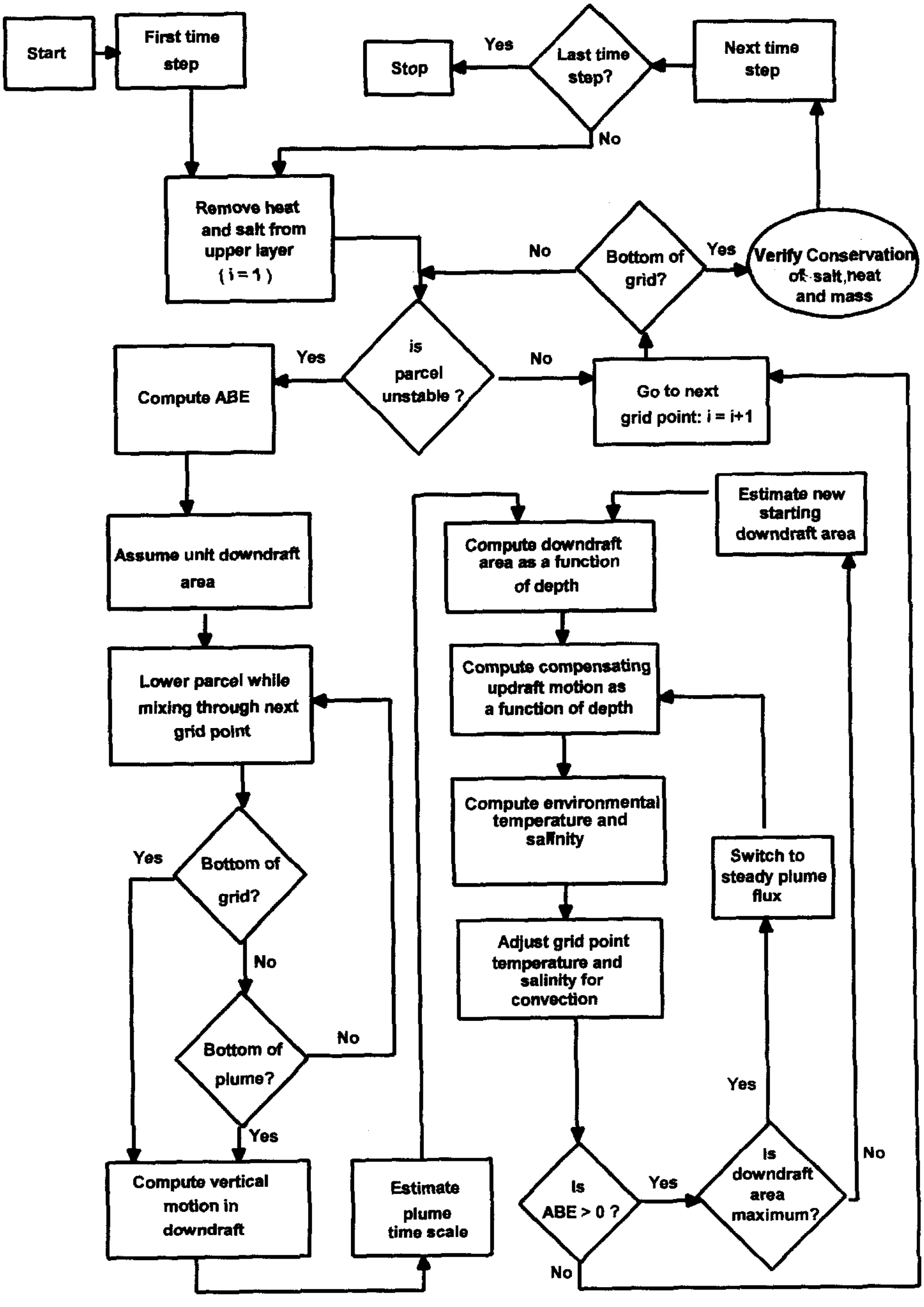

Fig. 6. Flow chart of the OPPS model as it is currently configured for stand-alone test runs.

not remove all the ABE, but only produces a reduction. A new estimate for $\sigma_p(1)$ is obtained from

$$\sigma_p(1)^{n+1} = \sigma_p(1)^n \frac{\text{ABE}^{n-1}}{(\text{ABE}^n - \text{ABE}^{n-1})} \tag{27}$$

where n is the iteration number. The iteration is repeated until all the ABE is removed, or until $\sigma_p(1)$ reaches a specified maximum value (currently set to 0.8).

If $\sigma_p(1)$ is 'pegged' at its maximum value, the code switches to a steady plume iterative loop, during which a plume mass flux occurs for a plume time scale τ_p. This time scale is adjusted iteratively as in Eq. (27) until the ABE is reduced to zero.

After the adjustment occurs for a given unstable layer, the next lowest layer is checked for stability, until the bottom of the grid is reached. If any adjustment has occurred, the total salt, heat, and mass are recomputed to verify conservation and the model moves to the next time step.

4. OPPS model results and benchmark tests

The OPPS was first configured as a one-dimensional, stand-alone model to facilitate testing and then was incorporated into the Parallel Ocean Circulation Model (POCM) as a parameterization, replacing the convective adjustment scheme. The OPPS was tested for consistency with analytical results and observations. First, simple tests of OPPS against theory and data are presented. These results are followed by a comparison with other models of varying complexity. The OPPS was tested using data from the Greenland Sea, the Weddell Sea, the Labrador Sea, and the MEDOC region. In each of these cases, we examined the OPPS simulations to determine whether a mixed layer formed that was consistent with climatology. In general, climatologically consistent mixed-layer depths were produced. From these tests we present several that demonstrate the strengths and weaknesses of OPPS. In addition, the suite of tests presented was chosen for oceanographic regions that are strongly influenced by mixing on the plume scale, in contrast to regions such as the MEDOC, where the small-scale eddies and the chimney can be the dominant features. This is not to say that OPPS will not mix appropriately in the MEDOC region, but that the Greenland Sea provides a stricter test that includes the contribution to the physics from the thermobaric effect.

The ability to convectively deepen a mixed layer at the appropriate time scale was tested by evaluating the mixed-layer deepening as a function of time against a stable salt gradient. Although these particular conditions have limited applicability in the ocean, this is a valuable test case with an analytical solution that has been verified with laboratory experiments (Turner, 1973 Eq. (8.2.4)). The mixed layer deepens against stratification at a rate proportional to $t^{1/2}$ (Fig. 7) as predicted by the analytical solution. Consequently, this leads to confidence that in the simple case of convective adjustment the OPPS should perform correctly.

The strictest test of OPPS was to determine whether the parameterization could generate mixed layers with the correct depth and hydrographic properties on an

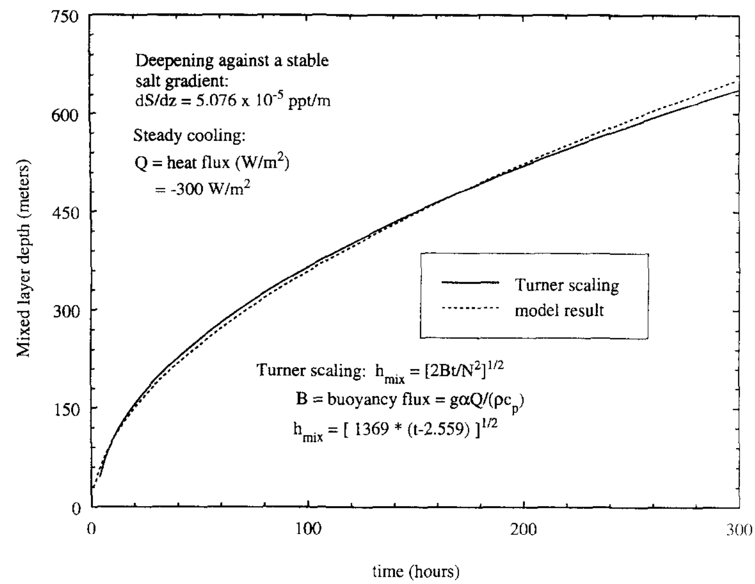

Fig. 7. Mixed-layer deepening against a stable salt gradient under cooling of $-300\,\mathrm{W\,m^{-2}}$ heat flux.

appropriate time scale. To accomplish this test, we identified an appropriate data set that had captured convectively driven mixed-layer deepening. The data are from the Greenland Sea Project (GSP) Station D-6 (GSP Group, 1990). Potential temperature and salinity profiles were collected at three different times showing the evolution of a deep mixed layer. These data were subsampled to reproduce a vertical resolution similar that used in model runs by Semtner and Chervin (1988). We initialized the OPPS model with the potential temperature and salinity from February 1989 data and then simulated the evolution of the deep mixing. The model was forced only by heat fluxes; the wind speeds during December were strong (Roach et al., 1993), followed by spells of cold, dry wind flowing from the north via the ice (Schott et al., 1993). The heat losses were estimated at greater than $500\,\mathrm{W\,m^{-2}}$ with a mean of $248\,\mathrm{W\,m^{-2}}$; the sensible heat flux was estimated at $99\,\mathrm{W\,m^{-2}}$ and the mean evaporative heat flux was $72\,\mathrm{W\,m^{-2}}$. Based on these values from Schott et al. (1993) and estimates from the ECMWF data, we used $-300\,\mathrm{W\,m^{-2}}$ heat flux with $-110\,\mathrm{W\,m^{-2}}$ for the latent heat flux.

Fig. 8 illustrates that the simulated potential temperature and salinity at 1000 m are in good agreement with observations. The OPPS reproduces the evolution of the salinity field; however, the potential temperatures in the upper 500 m are too low. The limitations of running OPPS as a one-dimensional model with only convective forcing are clearly seen in the upper 500 m. The temperature and the details in the structure were not reproduced as accurately as we had hoped, but the OPPS did produce the correct mixed-layer depth and deeper temperature structure, and salinity structure. This comparison might also look very different with a grid-point average of observations (if enough observations existed). An additional consideration is that the time series of profiles that was used does not necessarily represent the evolution from the first profile; conse-

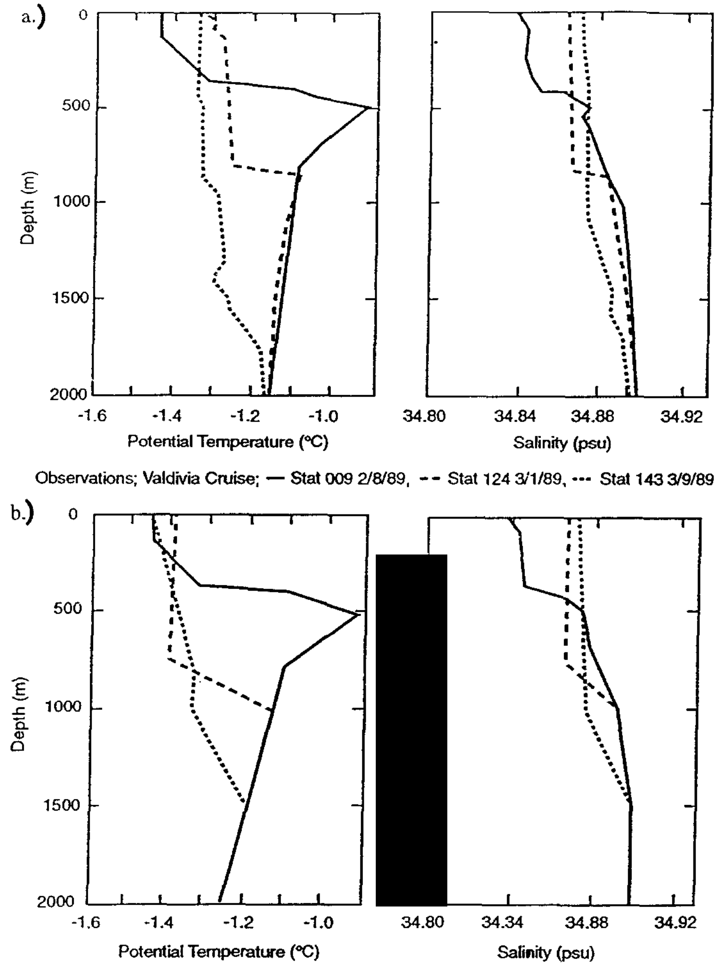

Fig. 8. The evolution of the potential temperature and salinity profiles as (a) observed on the Valdivia Cruise by the GSP Group at Station D-6 (GSP Group, 1990) and (b) as simulated by OPPS when initialized with the 8 February 1989 profiles and cooled with $-300\,\mathrm{W\,m^{-2}}$ heat flux and $110\,\mathrm{W\,m^{-2}}$ latent heat flux.

quently, we are not really comparing like measurements. These considerations are minor when compared with the general unreality of making one-dimensional comparisons where three-dimensional dynamics are active.

The OPPS was tested further by comparison with average fields from the three-dimensional LES model results of Denbo and Skyllingstad (1996). The Ocean Large Eddy Simulation Model (OLEM) was initialized with hydrographic sections from the Greenland Sea, as was OPPS, and the time evolution was compared. The comparison with this model gave insight into the ability to simulate strong thermobaric events and the detailed structure of the deepest mixing. The potential temperature and salinity profile from a hydrographic station (CTD 65) in the central Greenland Sea (2°W, 74°45′N), as reported by Rudels et al. (1989), were used for this test. This profile has characteristics of hydrographic structure that make it thermobarically unstable: cold fresh water overlying warm salty water. Both models were uniformly initialized with this data and then were forced with a heat flux of $-300\,\mathrm{W\,m^{-2}}$ and a latent heat flux of $-110\,\mathrm{W\,m^{-2}}$. The configuration of OLEM and a description of the LES simulation have been discussed at length by Denbo and Skyllingstad (1996).

The models were run for 10 days, and the three-dimensional results were averaged over latitude and longitude to produce a time evolution as a function of depth. In both simulations, the convective mixed layer deepens gradually for 4 days, then penetrative convection occurs, mixing and cooling the water column to depths of 1000–1200 m. The depth of penetration, evolution of the properties, and the time scale of the onset all

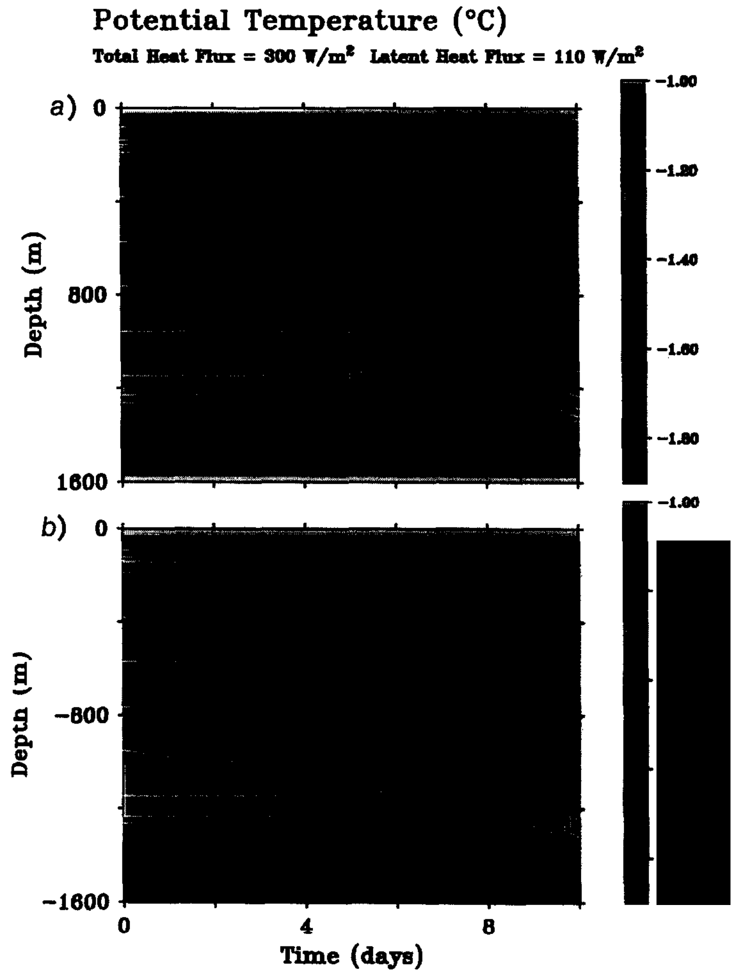

Fig. 9. (a) The evolution of the horizontally averaged potential temperature from the LES model (Denbo and Skyllingstad, 1996) initialized with a Greenland Sea hydrographic profile, and (b) the evolution of potential temperature from OPPS, initialized with the same hydrographic profile. Both models used cooling with $-300\,\mathrm{W\,m^{-2}}$ heat flux and $110\,\mathrm{W\,m^{-2}}$ latent heat flux.

compared favorably between the two model simulations (Fig. 9). The Denbo and Skyllingstad three-dimensional results show plumes of colder water penetrating through regions of stably stratified water. The plume diameter is nearly constant with depth, in agreement with the results presented in Section 2, as prescribed by Eq. (10). Denbo and Skyllingstad also showed that the effect of including rotation is to produce slanted plumes with smaller diameters when rotation is included (250–300 m), and larger plumes when rotation is neglected (450–500 m). In compensation for the strong downward vertical velocity in the plumes, there is a compensating upward flow that

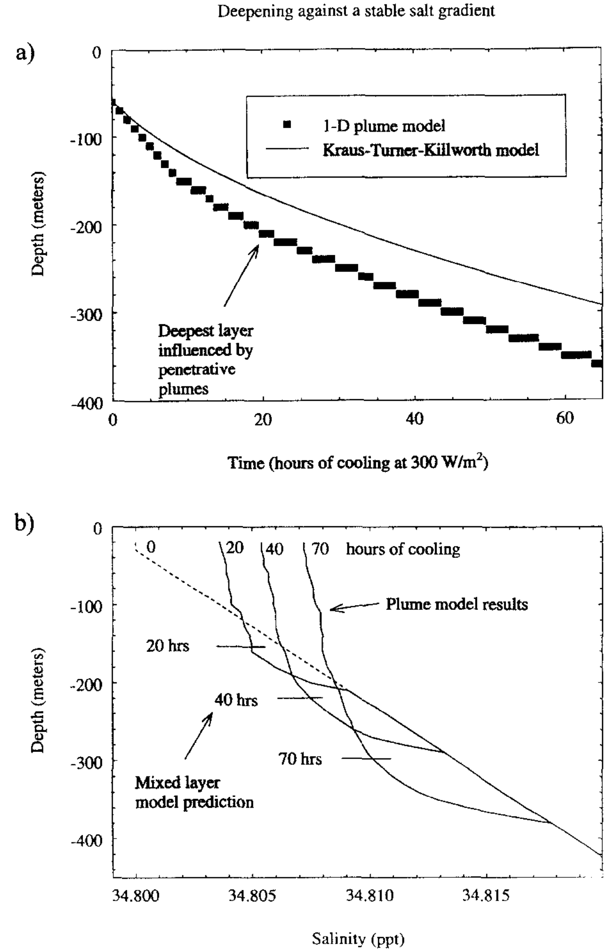

Fig. 10. Mixed-layer depth using the Kraus–Turner style model from Killworth (1985) compared with the mixed-layer depth from OPPS as measured by the deepest layer influenced by penetrative plumes. A stable, non-thermobaric profile with a constant temperature and a linear salt gradient was used and the simulation was cooled with $-300\,\mathrm{W\,m^{-2}}$ heat flux. In (a), the continuous line is the KTK prediction, and the heavy boxes are the OPPS prediction. In (b), the lines are salinity profiles at 20, 40 and 70 h; the KTK predictions are indicated by continuous lines.

eventually causes the $-1.35°C$ and colder isotherms to turn upward. In the OPPS simulation, the effect of the plumes is parameterized, and the consequent mixing is sufficiently effective to produce the same vertical structure and timing of deep penetrative convection. However, the vertical structure after 8–9 days is different from the three-dimensional results because of the three-dimensional circulation in the LES model.

Because of the thermobaric effect, mid-depth instabilities provide an increase in the vertical velocity and the entrainment rate (Garwood et al., 1994). Ultimately, this variation with depth of the entrainment rate has an effect on the mixing and the depth to which hydrographic properties are found. In certain cases, such as in the MEDOC region vs. Arctic regions, convected waters appear to be more homogeneous; this is especially true after chimneys have formed and the individual convective elements are no longer evident. In the Arctic regions, one sees bottom depth maxima of tracers (i.e. Fig. 1 of Rudels et al. (1989)). The depth varying entrainment rate in OPPS leads to partial mixing, and the parcel model approach facilitates the deposition of waters at deep levels of neutral stability. In contrast, traditional mixed-layer growth gives total mixing with homogenized water properties as a result. Without the thermobaric effect, the entrainment rate gives traditional mixed-layer growth; thus, the features of the MEDOC and of convective mixed layers are also simulated.

The parameterization was tested against existing vertical mixing parameterizations, such as the buoyancy-forced mixed-layer model of Killworth (1985). This model is a

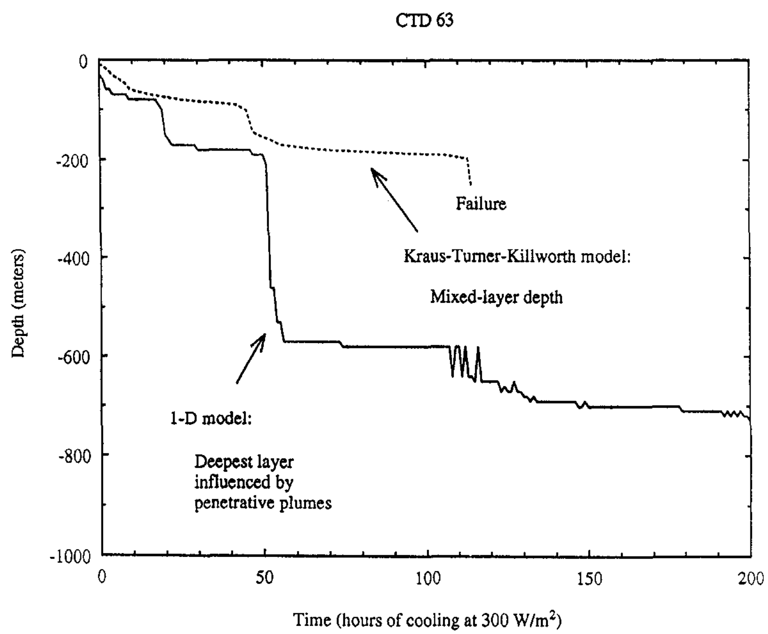

Fig. 11. The evolution of the mixed-layer depth using the Kraus–Turner style model from Killworth (1985) (dotted line) compared with the mixed-layer depth from OPPS as measured by the deepest layer influenced by penetrative plumes. A thermobaric profile (CTD 65 from Rudels et al. (1989)) was used and was cooled with $-300\,W\,m^{-2}$ heat flux.

Kraus–Turner type mixed-layer model (Kraus and Turner, 1967) that was reformulated to be convectively forced. The model (which we will call the Kraus–Turner–Killworth or KTK model) deepens the mixed layer under the influence of buoyancy forcing and, using a vertical integration through the mixed layer, predicts the depth of the mixed layer and the evolving potential temperature and salinity as a function of time. The KTK model does not have a penetrative bottom boundary condition. The OPPS model compared well with the KTK model under general conditions of buoyancy forcing in a non-thermobaric regime. Fig. 10 shows a comparison of the two model results for

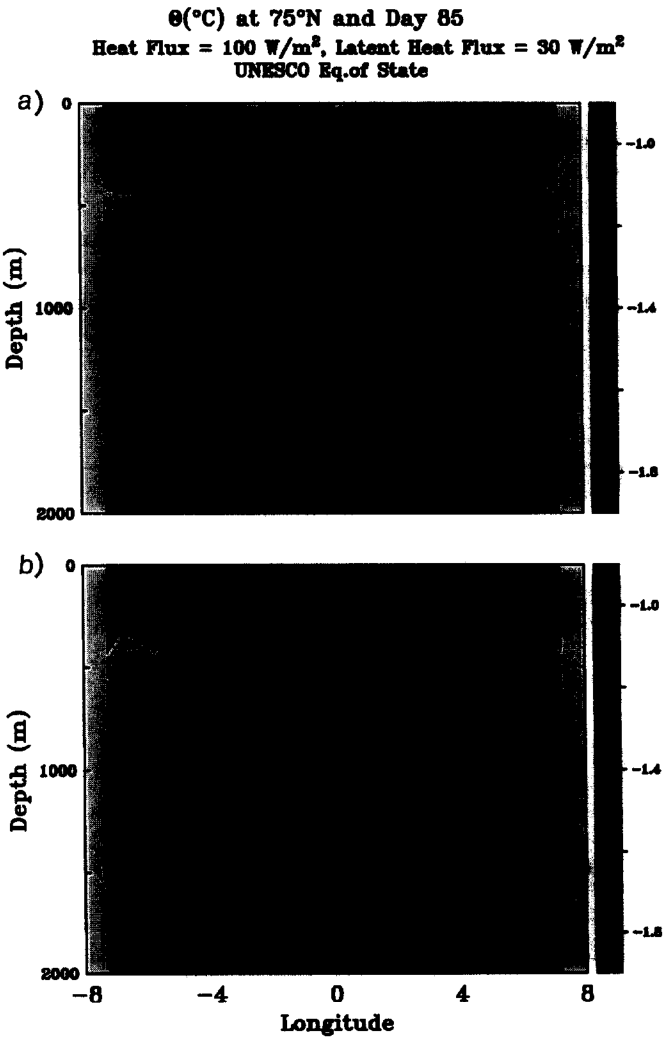

Fig. 12. A depth vs. latitude slice at 75°N of potential temperature from (a) POCM with OPPS and (b) POCM with the standard convective adjustment scheme. The section was taken on Day 85 of a 100day simulation. The simulation was forced with a cyclonic wind stress for 50days then cooling was initiated. In addition to the wind, the ocean was cooled with a heat flux of $-100 \mathrm{W m^{-2}}$ and a latent heat flux of $-30 \mathrm{W m^{-2}}$.

cooling against a stable salt gradient. In general, the OPPS penetrated slightly deeper than but at the same rate as the KTK. We believe the entrainment physics facilitate the penetrative deepening at the base of the mixed layer in the OPPS. Both models were compared under strongly thermobaric conditions (using CTD 65 as described above). The KTK was unable to simulate thermobaric penetrative convection; however, the OPPS model predicted the evolution of a deep penetrative convective mixed layer (Fig. 11).

Finally, the one-dimensional parameterization was incorporated into POCM. POCM, with OPPS incorporated, was run in a highly simplified Nordic Sea test basin and compared with a 'twin' POCM experiment that uses the standard convective adjustment algorithm. The tests were forced with a cyclonic wind field and $-100\,\mathrm{W\,m^{-2}}$ cooling with a latent heat flux of $-30\,\mathrm{W\,m^{-2}}$ to help create a preconditioned circulation. The resolution of the simulations was $1/4° \times 1/4° \times 16$ vertical levels. Tests to date of the POCM with OPPS show that penetrative convection occurs, and there is less homogenization of the intermediate levels than with the standard adjustment scheme (Fig. 12). These initial results show that convection occurs preferentially under the preconditioned doming that occurs in the simulation using OPPS. In the simulation with the standard convective adjustment scheme, the adjustment occurs in the vicinity of the thermocline, little doming forms, and the convection is triggered by spurious vertical velocities along the boundary of the domain. Without the triggering effect, the old convective adjustment scheme takes much longer to begin the process of convectively forced mixed-layer deepening. A future paper will discuss the comparison of these OGCM and more extensive OGCM simulations that are being performed to evaluate the effectiveness of the parameterization.

5. Discussion

The present convective adjustment schemes do not produce realistic vertical density structure, do not create the correct quantity of deep water, and do not use a time scale of adjustment that is in agreement with tracer ages or observations (Bacastow, 1988; Killworth, 1989; Skyllingstad et al., 1991). Marotzke (1991) found that the parameterization of convection has an impact on the steady state obtained in numerical simulations of thermohaline circulation. In addition, the choice of convective adjustment scheme has a larger influence on the results from models using mixed boundary conditions as opposed to models using restoring boundary conditions. Motivated by the need to better parameterize deep penetrative convection in climate models, we developed a convective adjustment scheme (OPPS) that parameterizes the entrainment and vertical mixing that result from penetrative convectively forced plumes. Under non-thermobaric conditions, OPPS performs appropriately for convective mixed-layer deepening.

The parameterization scheme takes the temperature and salinity profiles of OGCM grid boxes and simulates the subgrid-scale effects of convection using a one-dimensional parcel model. The one-dimensional model moves water parcels from the surface layer down to their level of neutral buoyancy, simulating the effect of convective plumes. While in transit, the plumes exchange water with the surrounding environment; however, the bulk of the plume water mass is deposited at the level of neutral buoyancy. Weak upwelling around the plumes is included to maintain an overall mass balance. The process continues until the negative buoyant energy of the one-dimensional vertical column is minimized. A full equation of state is used in both the plume model and entrainment rate calculation, thereby accounting for the thermobaric instabilities that can occur. The depth-dependent plume entrainment rate, which plays a central role in the model physics, is calculated using modified equations based on Turner's entrainment hypothesis (Turner, 1973). After the adjustment is complete, the weighted average of the state variables (between plume and environment) is returned to the OGCM. This scheme differs from the convective adjustment techniques currently used in OGCMs, because the parcels penetrate downward with the appropriate degree of mixing with the environment until they reach their level of neutral stability.

The OPPS was tested against observations by initializing the model with hydrographic data from the Greenland Sea (GSP Station D-6) and then simulating the evolution of hydrography (Fig. 8). The depth and strength of the mixing was correctly simulated, creating an appropriately deep mixed layer on the appropriate time scale. The parameterization was compared with the LES model results of Denbo and Skyllingstad (1996). The LES model and OPPS were initialized with hydrographic sections from the Greenland Sea, and the time evolution of mixing was compared. The comparison with this model gave insight into the ability to simulate strong thermobaric events. The depth of penetration, evolution of the properties, and the time scale of thermobaric convection compared favorably (Fig. 9). Finally, the parameterization was tested against existing vertical mixing parameterizations, such as the KTK buoyancy-forced mixed-layer model (Killworth, 1985). The OPPS model compared well with the KTK model under general conditions and was able to perform under strongly thermobaric conditions, whereas KTK failed under thermobaric conditions.

Results of the model tests support the hypothesis that thermobaric effects can have large impacts on the nature of oceanic convection. For example, when penetrative thermobaric plumes are simulated, the vertical temperature and salinity profiles created by the model can change rapidly at depth without showing major changes in the intermediate water. These results agree with high-resolution simulations of thermobaric plumes and hydrographic data for the Nordic seas, which show evidence of penetrative motion of surface water properties. For non-thermobaric plumes, the behavior of the model is similar to classic mixed-layer growth, with the mixed layer increasing in depth in proportion to the cooling rate.

The performance of the parameterization in a OGCM for deep convection as well as for any other convective adjustment need is now being tested. We are working on results in two areas: computational performance and correctness of water mass formation. The parameterization, tested in a simplified regional model, runs 7% slower than the OGCM using the standard Cox formulation of the convective adjustment scheme. This figure represents the overall runtime penalty and not the CPU difference per time step. This type of performance measure (overall run time difference) was calculated to recognize that the way in which the instabilities are removed has cascading effects; in OGCM runs with OPPS, fewer instabilities are generated. By observing close interval frames from the simulation, we were able to identify that the standard convective adjustment scheme 'overadjusts'; as a consequence, the neighboring grid boxes must then adjust. With the OPPS as a convective adjustment scheme, stability is reached faster with less of a change needed. This is because the weighted average allows for partial mixing. More tests are needed to determine the level of improvement or physical correctness that this faster adjustment brings about. We also realize that the comparisons against the standard adjustment scheme are comparisons against the slowest of convective adjustment schemes, and in our tests, we used ten scans to assure complete adjustment. Additional comparisons with the 'faster schemes', such as those described by Yin and Sarachik (1994), are needed.

The parameterization's potential as an improved convective adjustment scheme for achieving deep convection is being tested in the following way. We have incorporated the parameterization in the Arctic Ocean model of Maslowski (1994), and we are running multiple-year simulations. From these results, we will analyze the temperature and salinity census and tracer time scale. Even with existing convective adjustment methods, the objective measures that separate the role and effect of convective mixing from errors introduced by boundary conditions, forcing, unrepresentative lateral advection, and the myriad other problems that exist in OGCMs are difficult to identify. We are attempting to isolate some factors that will represent the role of convective mixing, such as water mass formation in the Arctic basins. The presentation of these results in this paper is not possible without greatly increasing the length.

In developing this parameterization, the simplest conceptual model of convection was used, where the unstable distribution of mass in the vertical direction was examined and where the vertical is the direction of gravitational acceleration. In the atmosphere, there is a form of convection that arises owing to the unstable distributions of angular momentum along the vector of the centrifugal acceleration. Emanuel (1994) described this as 'slantwise' convection. The major difference (in the atmosphere) between vertical convection (gravitational) and slantwise convection (centrifugal) is the direction of the convection and the nature of the conserved quantities. The slantwise convection is driven by angular momentum fluxes, whereas the vertical convection is driven by fluxes of heat and salt. To develop the ocean analog requires further research, especially the consideration of the interplay of lateral instabilities generated along the effective mixing zones.

In our parameterization, the mean vertical velocity in a grid column is assumed to be zero, which implies that there is no convergence near the ocean surface, and no outflow of deep water at the bottom. Therefore, the vertical adjustment in each grid column is essentially decoupled from adjacent grid columns. In regions of intense cooling, groups of adjacent convecting grid columns will form, yielding convecting patches, or 'chimneys'. Horizontal imbalances between adjacent grid columns, which could result in 'rim currents' and other mesoscale events, such as baroclinic instability and slumping, and which could be important in slantwise convection, are not handled by OPPS. These are now left to be resolved by the OGCM and induced, in part, by the adjusted density that OPPS calculates.

The effects (if any) of lateral transfer by these larger structures, such as rim current eddies, on the details of the deep vertical mixing process are not parameterized by OPPS. Parameterizing the effects of evolving and slumping chimneys on a horizontal space scale smaller than the OGCM horizontal grid spacing is a separate research problem.

Of the other deep convection parameterizations that have been developed, that of Alves (1995) is the most similar, but there are still significant differences. OPPS was originally designed for use in an OGCM, and therefore, certain choices were made that would facilitate efficient operation, such as complete (or near complete) removal of instabilities. Alves (1995) allowed for instabilities to remain by using an unstable layer spanning several model layers. In addition, the Alves scheme has included detrainment physics. The major differences are related to the way the closure schemes are formulated and applied. This scheme holds great promise, and a comparison would be a valuable addition to deep convection parameterization research.

Acknowledgements

This research was supported by the CHAMMP Program, under D. Bader and M. Riches, at the US Department of Energy (DOE) under Contract DE-AC06-76RLO 1830. Pacific Northwest National Laboratory is operated for DOE by Battelle Memorial Institute. The authors would like to thank the reviewers; their comments and suggestions improved the paper. We thank Dr. D. Denbo for insightful discussions and suggestions in the development of this work and for sharing his model results, Dr. E. Skyllingstad for his helpful review and advice during the progress of the research, Dr. M. Visbeck for sharing the GSP D-6 data, Dr. G. Holloway for stimulating debates, L. Hibler for his contributions to the OGCM simulations, and Dr. S. Thomas for her assistance in editing and reviewing the paper.

Appendix A. Notes on the technical derivation

We start with the basic equations:

$$\frac{\mathrm{d}M}{\mathrm{d}z} = 2\alpha w_\rho b \rho_\mathrm{e} \tag{A1}$$

$$M = b^2 w_\rho \rho_\rho \tag{A2}$$

$$\frac{\mathrm{d}(M w_\rho)}{\mathrm{d}z} = g b^2(\rho_\rho - \rho_\mathrm{e}) \tag{A3}$$

where b is the plume radius, w_p is the plume vertical velocity, α is the entrainment constant, M is the plume mass flux, ρ_p is the density of the plume, z is the vertical coordinate, ρ_e is the density of the environment, and g is the gravitational acceleration.

These can be combined to give ($\rho_\mathrm{p}/\rho_\mathrm{e} \approx 1$)

$$\frac{\mathrm{d}b}{\mathrm{d}z} = 2\alpha - \frac{gb(\rho_\mathrm{p} - \rho_\mathrm{e})}{2\rho w_\mathrm{p}^2} - \frac{b}{2\rho}\frac{\mathrm{d}\rho}{\mathrm{d}z}$$

Scaling: term number

(1)	(2)	(3)	(4)
b/L_z	2α	$gb/2w_p^2(\Delta\rho/\rho)$	$b/L_z^{1/2}(\Delta\rho/\rho)$
$\Downarrow$	$\Downarrow$	$\Downarrow$	$\Downarrow$
b/L_z	2α	$bL_z/2w_p^2(N^2)$	$b/2g(N^2)$
$\Downarrow$	$\Downarrow$	$\Downarrow$	$\Downarrow$
0.2	0.2	$2.5\times10^6 N^2$	$5N^2$
	Entrainment	Acceleration	Nonhydro terms neglected

where

$$N^2 = \frac{-g}{\rho}\frac{\mathrm{d}\rho}{\mathrm{d}z} \approx \frac{g}{L_z}\frac{\Delta p}{\rho}$$

We pick $b \sim 100\,\mathrm{m}$, $L_z \sim 500\,\mathrm{m}$, $\alpha \sim 0.1$, $w_p \sim 0.1\,\mathrm{m\,s^{-1}}$, and $g \sim 10\,\mathrm{m\,s^{-1}}$. For thermobaric conditions, $N^2 \sim 10^{-8}$ or smaller, and Terms (1), (2), and (3) are about the same order of magnitude; Term (4) is eight orders of magnitude smaller than Term (3).

References

Aagaard, K. and Carmack, E.C., 1989. The role of sea ice and other fresh water in the Arctic circulation. J. Geophys. Res., 94: 14485–14498.

Alves, J.O.S., 1995. Open-ocean deep convection: understanding and parametrization. Ph.D. Thesis, University of Reading.

Bacastow, R., 1988. Circulation model of the ocean carbon cycle. US Department of Energy, Carbon Dioxide Research Division, Research Project of the Month, November 1988, Washington, DC.

Boubonov, B.M. and Golitsyn, G.S., 1990. Temperature and velocity field regimes of convective motions in a rotating plane fluid layer. J. Fluid. Mech., 219: 215–239.

Bryan, K., 1969. A numerical method for the study of the circulation of the world ocean. J. Comput. Phys., 4: 347–376.

Byers, H.E., 1951. Thunderstorms. Compendium of Meteorology. Am. Meteorol. Soc., Boston, MA, pp. 681–693.

Carmack, E.C., 1990. Large-scale physical oceanography of polar oceans. In: W.O. Smith, Jr. (Editor), Polar Oceanography, Part A, Physical Science. Academic Press, San Diego, CA, pp. 171–222.

Carsey, F. and Garwood, Jr., R.W., 1993. Identification of modeled ocean plumes in Greenland gyre ERS-1 SAR data. Geophys. Res. Lett., 20: 2207–2210.

Clarke, R.A. and Gascard, J.C., 1983. The formation of Labrador Sea water. I. Large scale processes. J. Phys. Oceanogr., 13: 1764–1778.

Cox, M.D., 1984. A primitive equation, three-dimensional model of the ocean. GFDL Ocean Group Tech. Rep. 1, GFDL–Princeton University, Princeton, NJ.

Deardorff, J.W. and Willis, G.E., 1985. Further results from a laboratory model of the convective planetary boundary layer. Boundary-Layer Meteorol., 32: 205–236.

Denbo, D.W. and Skyllingstad, E.D., 1996. An ocean large eddy model with application to convection in the Greenland Sea. J. Geophys. Res., 101: 1095–1110.

Emanuel, K.A., 1994. Atmospheric Convection. Oxford University Press, New York, 580 pp.
Fernando, H.J.S. and Ching, C.Y., 1993. Effects of background rotation on turbulent line plumes. J. Phys. Oceanogr., 23: 2125–2129.
Fernando, H.J.S., Boyer, D.L. and Chen, R., 1989. Turbulent thermal convection in rotating and stratified fluids. Dyn. Atmos. Oceans, 13: 513–547.
Fernando, H.J.F., Chen, R. and Boyer, D.L., 1991. Effects of rotation on convective turbulence. J. Fluid Mech., 228: 513–547.
Fritsch, J.M. and Chappell, C.F., 1980. Numerical prediction of convectively driven mesoscale pressure systems. 1. Convective parameterization. J. Atmos. Sci., 37: 1722–1733.
Garwood, R.W., 1991. Enhancements to deep turbulent entrainment. In: P.C. Chu and J.C. Gascard (Editors), Deep Convection and Deep Water Formation in the Oceans. Elsevier, Amsterdam, 382 pp.
Garwood, R.W., Isakari, S.M. and Gallacher, P.C., 1994. Thermobaric convection. Geophys. Monogr. Am. Geophys. Union, 85: 199–209.
Gascard, J.C., 1991. Open ocean convection and deep water formation revisited in the Mediterranean, Labrador, Greenland and Weddell Seas. In: P. Chu and J. Gascard (Editors), Deep Convection and Deep Water Formation in the Oceans. Elsevier, Amsterdam, pp. 157–181.
Gascard, J.C. and Clarke, R.A., 1983. The formation of Labrador Sea water. II. Mesoscale and smaller-scale processes. J. Phys. Oceanogr., 13: 1779–1797.
Gill, A.E., 1982. Atmosphere–Ocean Dynamics. Academic Press, New York, 662 pp.
Gordon, A., 1978. Deep convection west of Maude Rise. J. Phys. Oceanogr., 8: 600–612.
GSP Group, 1990. Greenland Sea Project. EOS, Trans. Am. Geophys. Union, 71: 750–755.
Guest, P.S. and Davidson, K.L., 1991. Meteorological triggers for deep convection in the Greenland Sea. In: P. Chu and J. Gascard (Editors), Deep Convection and Deep Water Formation in the Oceans. Elsevier, Amsterdam, pp. 369–375.
Heinze, C., Schlosser, P., Koltermann, K.P. and Meincke, J., 1990. A tracer study of the deep water renewal in the European polar seas. Deep-Sea Res., 37: 1425–1453.
Holland, W.R., 1979. The general circulation of the ocean and its modeling. Dyn. Atmos. Oceans, 3: 111–142.
Johannessen, O.M., Sandven, S. and Johannessen, J.A., 1991. Eddy related winter convection in the Boreas Basin. In: P. Chu and J. Gascard (Editors), Deep Convection and Deep Water Formation in the Oceans. Elsevier, Amsterdam, pp. 87–106.
Jones, H. and Marshall, J., 1993. Convection with rotation in a neutral ocean: a study of open-ocean deep convection. J. Phys. Oceanogr., 23: 1009–1039.
Jonsson, S., 1991. Seasonal and interannual variability of wind stress curl over the Nordic Seas. J. Geophys. Res., 96: 2649–2659.
Kessler, E., 1988. Thunderstorm Morphology and Dynamics. University of Oklahoma Press, Norman, pp. 317–321.
Killworth, P.D., 1979. On chimney formations in the ocean. J. Phys. Oceanogr., 9: 531–554.
Killworth, P.D., 1983. Deep convection in the world ocean. Rev. Geophys. Space Phys., 21: 1–26.
Killworth, P.D., 1985. A two-level wind and buoyancy driven thermocline model. J. Phys. Oceanogr., 15: 1414–1432.
Killworth, P.D., 1989. On the parameterization of deep convection in ocean models. In: P. Muller and D. Henderson (Editors), Parameterization of Small-Scale Processes. Proc. 'Aha Huliko'a Hawaiian Winter Workshop, Hawaii Institute of Geophysics, University of Hawaii, Honolulu, HI, pp. 59–74.
Kraus, E.B. and Turner, J.S., 1967. A one-dimensional model of the seasonal thermocline. II: The general theory and its consequences. Tellus, 19: 98–106.
Kuo, H.L., 1974. Further studies of the parameterization of the influence of cumulus convection on large-scale flow. J. Atmos. Sci., 31: 1232–1240.
Leaman, K.D. and Schott, F.A., 1991. Hydrographic structure of the convection regime in the Gulf of Lions: winter 1987. J. Phys. Oceanogr., 21: 575–598.
List, E.J., 1982. Turbulent jets and plumes. Annu. Rev. Fluid Mech., 14: 189–212.
Madec, G. and Crepon, M., 1991. Thermohaline-driven deep water formation in the northwestern Mediterranean Sea. In: P. Chu and J. Gascard (Editors), Deep Convection and Deep Water Formation in the Oceans. Elsevier, Amsterdam, pp. 241–265.

Marotzke, J., 1991. Influence of convective adjustment on the stability of the thermohaline circulation. J. Phys. Oceanogr., 21: 903–907.

Maslowski, W., 1994. Numerical modeling study of the circulation of the Greenland Sea. Ph.D. Thesis, University of Alaska, Fairbanks, 198 pp.

Maxworthy, T. and Narimousa, S., 1994. Unsteady deep convection in a homogeneous rotating fluid. J. Phys. Oceanogr., 24: 865–887.

Muench, R., 1991. Relic convective features in the Weddell Sea. In: P. Chu and J. Gascard (Editors), Deep Convection and Deep Water Formation in the Oceans. Elsevier, Amsterdam, pp. 53–69.

Paluszkiewicz, T., Garwood, R.W. and Denbo, D.W., 1994. Deep convective plumes in the ocean. Oceanography, 7: 37–44.

Rhein, M., 1991. Ventilation rates of the Greenland and Norwegian seas derived from distributions of the chlorofluoromethanes F11 and F12. Deep-Sea Res., 38: 485–503.

Roach, A.T., Aagaard, K. and Carsey, F., 1993. Coupled ice–ocean variability in the Greenland Sea. Atmos.-Ocean, 31: 319–337.

Rudels, B., Quadfasel, D., Friedrich, H. and Houssais, M.-N., 1989. Greenland Sea convection in the winter of 1987–1988. J. Geophys. Res., 94: 3223–3227.

Sander, J., Wolf-Gladrow, D. and Olbers, D., 1995. Numerical studies of open ocean deep convection. J. Geophys. Res., 100: 20579–20600.

Sankey, T., 1973. The formation of deep water in the northwestern Mediterranean. Prog. Oceanogr., 5: 159–179.

Schott, F. and Leaman, K.D., 1991. Observations with moored acoustic doppler current profilers in the convective regime in the Golfe du Lion. J. Phys. Oceanogr., 21: 558–574.

Schott, F., Leaman, K.D. and Zika, R.G., 1988. Deep mixing in the Gulf of Lions, revisited. Geophys. Res. Lett., 15: 800–803.

Schott, F., Visbeck, M. and Fischer, J., 1993. Observations of vertical currents and convection in the Central Greenland Sea during the winter of 1988–1989. J. Geophys. Res., 98: 14402–14421.

Schott, F., Visbeck, M. and Send, U., 1994. Open ocean deep convection, Mediterranean and Greenland Seas. In: P. Malanotte-Rizzoli and A.R. Robinson (Editors), Ocean Processes in Climate Dynamics: Global and Mediterranean Examples. Kluwer Academic, Dordrecht, 437 pp.

Scott, J.C. and Killworth, P.D., 1991. Upper ocean structures in the south-western Iceland Sea: a preliminary report. In: P. Chu and J. Gascard (Editors), Deep Convection and Deep Water Formation in the Oceans. Elsevier, Amsterdam, pp. 107–121.

Semtner, A.J., 1974. An oceanic general circulation model with bottom topography. Numerical simulation of weather and climate. Tech. Rep. 9, Dept. Meteorol., UCLA, 99 pp.

Semtner, A.J. and Chervin, R.M., 1988. A simulation of the global ocean circulation with resolved eddies. J. Geophys. Res., 93: 15502–15522.

Send, U. and Marshall, J., 1995. Integral effects of deep convection. J. Phys. Oceanogr., 25: 855–872.

Skyllingstad, E.D., Denbo, D.W. and Downing, J., 1991. Convection in the Labrador Sea: community modeling effort results. In: P. Chu and J. Gascard (Editors), Deep Convection and Deep Water Formation in the Oceans. Elsevier, Amsterdam, pp. 341–354.

Smith, N.R., 1989. The southern ocean thermohaline circulation: a numerical model sensitivity study. J. Phys. Oceanogr., 129: 713–726.

Solomon, H., 1974. Comments on the Arctic bottom water problem and high-latitude thermohaline sinking. J. Geophys. Res., 79: 881–884.

Squires, P. and Turner, J.S., 1962. An entraining jet model for cumulo-nimbus updraughts. Tellus, 14: 422–434.

Turner, J.S., 1962. The starting plume in neutral surroundings. J. Fluid Mech., 13: 356–368.

Turner, J.S., 1963. Model experiments relating to thermals with increasing buoyancy. Q. J. R. Meteorol. Soc., 89: 62–74.

Turner, J.S., 1973. Buoyancy Effects in Fluids. Cambridge University Press, Cambridge, 367 pp.

Turner, J.S., 1986. Turbulent entrainment: the development of the entrainment assumption, and its application to geophysical flows. J. Fluid. Mech., 173: 431–471.

Vaughn, S.L. and Leaman, K.D., 1995. The role of small-scale cells in the Mediterranean convection process. J. Phys. Oceanogr., 25: 2423–2436.

Visbeck, M., Fischer, J. and Schott, F., 1995. Preconditioning the Greenland Sea for deep convection: ice formation and ice drift. J. Geophys. Res., 100: 18489–18502.

Weaver, A.J. and Sarachik, E.S., 1991. The role of mixed boundary conditions in numerical models of the ocean's climate. J. Phys. Oceanogr., 21: 1470–1493.

Yin, F.L. and Sarachik, E.S., 1994. An efficient convective adjustment scheme for ocean general circulation models. J. Phys. Oceanogr., 24: 1425–1430.